ORIGINAL ARTICLE

lajss.org© Latin American Journal of Solids and Structures

www.lajss.org

Crash Failure Prediction of Lithium-ion Batteries Based on Finite Element and Machine Learning Methods

Yan Ma[a,b], Hongjun He[a,b], Ning Wang[a,b], Hongbin Tang[a,b], Hongxin Xia[a,b], Guang Chen[c,d], Zhongyuan Song[c,d*], Wenshuo Chen[c,d]

[a] FAW Global R&D Center, Changchun 130000, China. Email: mayan@faw.com.cn, hehongjun@faw.com.cn, wangning7@faw.com.cn, tanghongbin@faw.com.cn, xiahongxin@faw.com.cn

[b] National key Laboratory of Advanced Vehicle Integration and Control, Changchun 130000, China.

[c] School of Mechanical Engineering, Hebei University of Technology, Tianjin 300130, China. Email: chenguang@hebut.edu.cn, songzy1158140725@163.com, C18849276808@163.com

[d] Tianjin Key Laboratory of Power Transmission and Safety Technology for New Energy Vehicles, Tianjin 300130, China.

* Corresponding author

https://doi.org/10.1590/1679-7825/e8785

Abstract

The aging state and operational environment of lithium-ion batteries (LIBs) in electric vehicles are highly complex and variable. To investigate LIB safety under foreign object collisions, this study develops a detailed finite element model of 18650 LIBs at different cycle counts. Following model validation, we conduct comprehensive simulation tests using indenters of varying types, sizes, intrusion angles, and loading positions. A machine learning model is subsequently developed to rapidly predict battery failure displacement and load. Results demonstrate that this approach achieves high-accuracy prediction of LIB failure behavior, providing a valuable reference for other LIB application scenarios.

Keywords

Li-ion battery, Detailed computational model, Crash safety, Machine learning, Fast prediction

Graphical abstract

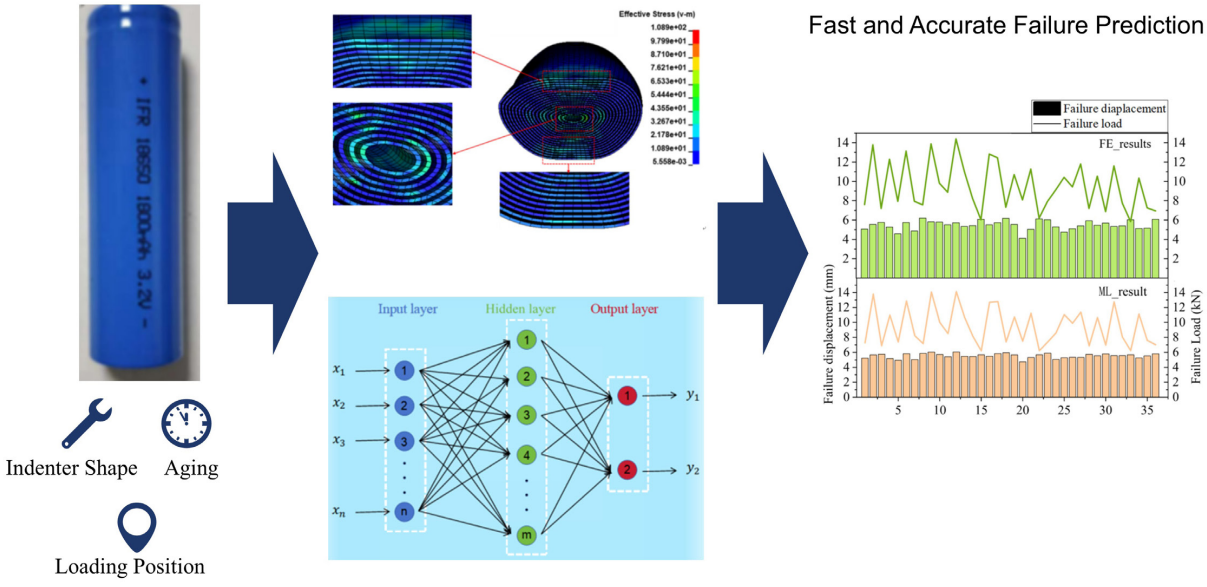

Received July 30, 2025. In revised form December 14, 2025. Accepted January 26, 2026. Available online January 28, 2026.
https://doi.org/10.1590/1679-7825/e8785

1 INTRODUCTION

The complex operating conditions of new energy vehicles demand battery modules capable of withstanding extreme mechanical stresses. Collision-induced foreign object intrusion into battery packs frequently occurs and may cause severe damage, including internal short circuits (ISCs). In extreme cases, such events can trigger battery module combustion, posing significant public safety risks(Feng X, Ouyang M, Liu X, et al,2018). Consequently, investigating the mechanical behavior of lithium-ion batteries (LIBs) under load is critical for ensuring safety and supporting sustainable development of electric vehicles.

The mechanical properties of battery components fundamentally determine LIB safety performance. Lai et al(2014). demonstrated through tensile testing that copper and aluminum foils provide the primary load-bearing capacity in electrodes, while graphite and $LiFePO_4$ coatings contribute minimally. Expanding on this work, Sahraei et al(Sahraei E, Bosco E, Dixon B, et al,2016;Sahraei E, Kahn M, Meier J, et al,2015). systematically characterized coating mechanical properties and investigated electrode material failure under localized stress using combined experimental and computational approaches. Zhang et al(2017). further advanced this understanding through comprehensive studies of electrode intrinsic behavior, developing accurate models of stress-strain response under uniaxial loading. Subsequent work by Zhang's team(Zhang X, Sahraei E, Wang K,2016) revealed important anisotropic characteristics of separators under uniaxial tension. Complementing these studies, Wang et al.(2022) established advanced theoretical and numerical models for battery casing materials under impact loading.

At the cell level, Wierzbicki et al(2013). conducted pioneering quasi-static tests on cylindrical and pouch LIBs, establishing clear correlations between mechanical abuse and short-circuit behavior. Their work identified the battery core as the primary contributor to mechanical resilience. Luo et al(Chung S.H, Tancogne J, Zhu,H,2018;Luo H, Xia Y, Zhou Q,2017). provided further insights through indentation tests that tracked damage evolution in pouch batteries at varying force levels. Li et al(2022). employed controlled three-point bending tests on prismatic cells, observing extensive electrode layer cracking without ISC occurrence in 75% of tested batteries - demonstrating that cracking and short-circuiting are distinct failure modes under bending loads.

Significant progress has been made in simulating battery mechanical behavior through finite element analysis. Campbell et al(2014). developed a homogenized 18650 cell model using LS-DYNA's collapsible foam formulation, successfully predicting load-displacement responses, deformation patterns, and short-circuit initiation during various mechanical tests (ball crush, plane crush, and three-point bending). Zhang et al(2015). advanced this work by implementing refined modeling techniques, creating an efficient quarter-cell model that accurately reproduced quasi-static indentation behavior with strong experimental correlation. Zhu et al(2016). further enhanced modeling fidelity through a detailed 18650 battery model that elucidated component-specific deformation mechanisms and localized short-circuit sites under compression.

The modeling paradigm was extended to pouch cells by Shraddha et al(2021)., who systematically evaluated different finite element approaches for spherical indentation simulations. Their work established critical benchmarks for replicating actual battery safety testing protocols. While these sophisticated models achieve excellent predictive capability, their computational intensity remains prohibitive for practical applications. Li et al.(2018) addressed this limitation by pioneering machine learning approaches to predict failure outcomes from impact scenarios, demonstrating the feasibility of rapid safety assessment while maintaining accuracy.

Battery aging significantly influences mechanical properties, as demonstrated by Liu et al.(2021) through low-temperature indentation tests on pouch cells. Their results revealed aging-induced rightward shifts in force-displacement curves alongside increased bending and peak forces. Qu et al.(2022) confirmed these findings, observing greater peak displacement in aged cells under indentation. At the material level, Ji et al.(2013) characterized the complex effects of cycling on electrode mechanical properties, showing that while tensile strength initially increases then decreases with cycling, compressive modulus exhibits different trends.

Based on the above background, this thesis aims to establish a refined model of the 18650 lithium-ion battery that can characterize different aging degrees of the battery. The model is validated under compression mechanical tests, and a short-circuit criterion for the battery is established based on the stress of the battery anode material in accordance with the test conditions. Additionally, to predict the rapid failure of the battery monomer under indentation conditions, a neural network is built based on the refined model. This neural network enables the rapid failure prediction of intruders with different shapes, sizes, angles, and positions intruding into the battery monomer. The prediction model is capable of predicting the failure displacement and failure load of the 18650 lithium-ion battery under localized compression conditions. Moreover, the research method described above can also predict the failure displacement and failure load of batteries under other conditions.

The structure of this paper is arranged as follows: First, tests are conducted on the internal components and cell monomers of the battery to obtain the mechanical properties of each component material and the battery monomers.

Then, based on the material properties of each component, a refined finite element model of the 18650 lithium-ion battery is established, a battery failure criterion is formulated, and the accuracy of the model is verified using single-cell experimental data. Finally, sample data are obtained through simulation tests, and a machine learning-based failure prediction model is constructed to quickly predict the failure displacement and load of the battery. Meanwhile, the accuracy and robustness of the model are verified.

2 EXPERIMENT

2.1 MATERIAL AND SPECIMEN PREPARATION

In this study, a commercial 18650 lithium iron phosphate battery is selected as the research object. Figure 1 illustrates the structure of this battery, with the anode thickness being 0.2 mm, the cathode thickness being 0.17 mm, and the diaphragm thickness being 0.02 mm. During the fabrication of lithium-ion battery electrodes, the active material is bonded to the metal collector. It is not feasible to completely separate the active material and the collector for individual testing. Therefore, only the electrodes and diaphragm are subjected to mechanical testing.

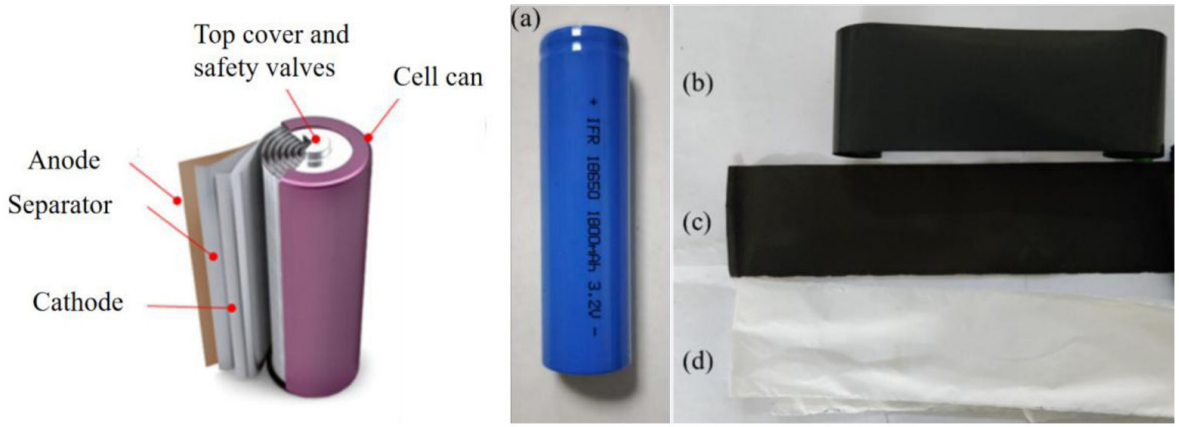

Figure 1. 18650 Li-ion battery: (a) li-ion battery cell; (b) cathode; (c) anode; (d) separator

After disassembling the battery using tools, the compression tests of the cathode, anode, and diaphragm are conducted respectively. The specimen size for the compression test is 20 mm × 20 mm. The cathode and anode are tested using a 20-layer stack with nominal thicknesses of 3.4 mm and 4 mm, respectively, while the diaphragm is compressed using a 60-layer stack with a nominal thickness of 1.2 mm.

2.2 EXPERIMENTAL AND SIMULATION

The quasi-static compression test is carried out using an electronic universal testing machine, with a transducer range of 100 kN and an accuracy of 2%. The prepared laminated specimens of the cathode, anode, and diaphragm are placed on the lower indenter of the testing machine, and a preload of 0.1 kN is applied to the specimens to eliminate the gap between the layers. The loading speed is set to 1 mm/min, and the tests are continuously loaded to a load of 80 kN (cathode) / 60 kN (or slope change) and then unloaded, with each set of tests performed ten times(Chung S.H, Tancogne J, Zhu,H,2018).

Figure 2 presents the force–displacement curves obtained from the cathode compression tests. The curves for the battery materials under three different cycle counts follow a consistent trend, which can be divided into two distinct stages. In the first stage, the reduction in coating porosity leads to a gradual hardening of the effective modulus, corresponding to the initial nonlinear response. This is followed by a linear densification stage, where the coating becomes fully compacted and displacement increases linearly with force.

To facilitate comparison across all samples, the force at a displacement of 0.8 was used as a reference point. At 0, 50, and 100 cycles, the force values (in kN) at this displacement were recorded in the ranges of (31.58, 39.74), (32.24, 40.74), and (31.45, 45.84), respectively, with corresponding ranges of 8.16, 8.50, and 14.39 kN. As the cycle number increased from 0 to 50, both the average force–displacement response and data scatter remained largely unchanged. In contrast, at 100 cycles, a marked increase in force value dispersion was observed compared to the lower cycle counts. These results suggest the existence of a critical cycle number beyond which the variability in mechanical properties becomes significantly more pronounced. Nevertheless, the average mechanical performance and its general trend remain largely unaffected by cycling. This observation aligns with findings from prior research indicating that neither the cathode coating nor the current collector experiences yielding or damage (Qi Y, Guo H, Hector L G, et al., 2010).

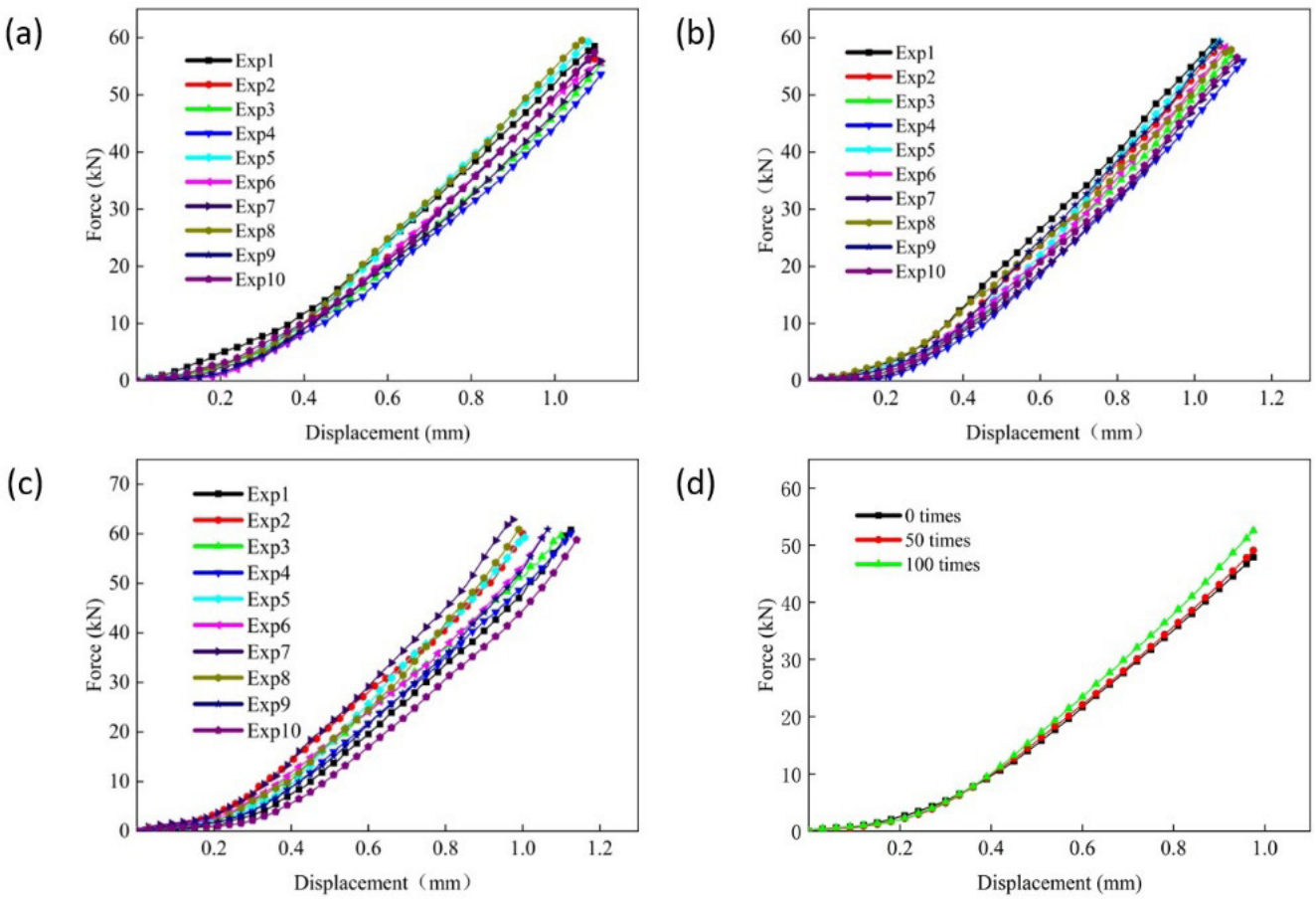

Figure 2 Force-displacement curves of cathode materials for batteries with different cycle times: (a) 0 cycles; (b) 50 cycles; (c) 100 cycles; (d) Comparison of different cycle times

Figure 3 presents the force-displacement curves of the anode compression tests. The number of cycles has a more significant impact on the mechanical properties of the anode material. When the load approaches 42 kN, the slope of the anode curve for new batteries changes, a phenomenon that may stem from the yielding of the metal current collector or the damage of the coating material. The anode failure loads of batteries with different cycle numbers vary significantly: the failure load decreases to 37 kN after 50 cycles and further drops to 32.5 kN after 100 cycles. This indicates that as the battery aging degree increases, the anode strength gradually decreases, making it more prone to compressive collapse.

Figure 3 presents the force–displacement curves obtained from the anode compression tests. The number of cycles exerts a more pronounced influence on the mechanical behavior of the anode material. In the case of 0 cycles batteries, a distinct change in the slope of the anode curve occurs as the load approaches 42 kN, which may be attributed to yielding of the metal current collector or damage to the coating material. The peak failure loads vary considerably with cycling, exhibiting a clear declining trend in the mean peak force as the number of cycles increases. Specifically, at 0, 50, and 100 cycles, the experimental peak force ranges are (42.02, 45.26) kN, (35.59, 39.23) kN, and (29.33, 34.12) kN, with corresponding ranges of 3.24, 3.64, and 4.79 kN, respectively. These results demonstrate that as battery aging progresses, the anode strength progressively declines, rendering it more susceptible to compressive collapse.

Figure 4 presents the force–displacement curves obtained from compression tests on diaphragm specimens. The curves don't demonstrate yielding during the compression process. The diaphragm exhibits a more pronounced force increase in the initial compression stage. As shown in Figure 4(d), which summarizes the compression test results under various cycling conditions, the average force–displacement curves after 0, 50, and 100 cycles show only minor variations. However, cycle number does influence the dispersion of mechanical properties. For example, at a displacement of 0.5, the diaphragm tensile force ranges are (20.67, 25.8) kN, (21.42, 24.36) kN, and (21.01, 28.59) kN for 0, 50, and 100 cycles, respectively, with corresponding ranges of 5.13 kN, 2.94 kN, and 7.58 kN. These values reflect a clear increase in mechanical dispersion at 100 cycles. Despite this, the diaphragm retains stable compressive mechanical properties throughout repeated cycling.

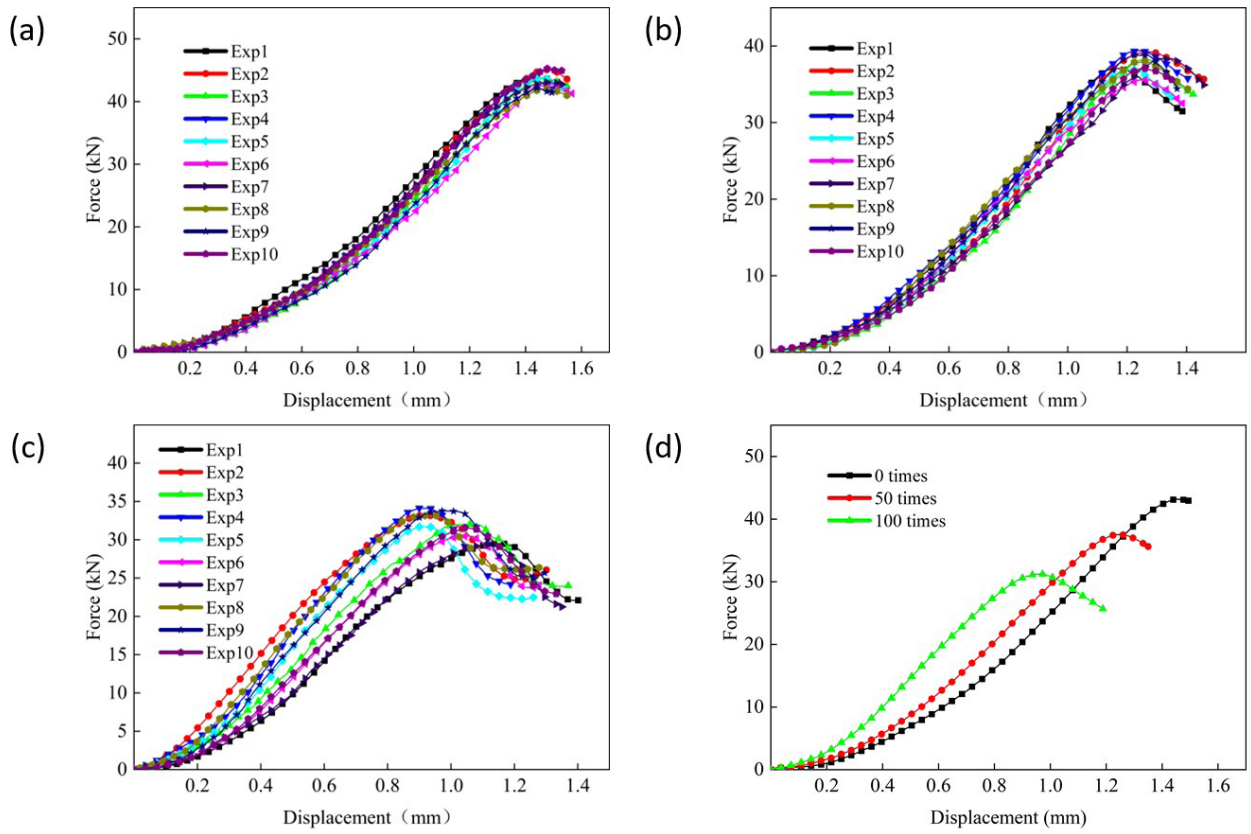

Figure 3 Force-displacement curves of anode materials of batteries with different cycle times: (a) 0 cycles; (b) 50 cycles; (c) 100 cycles; (a) Comparison of different cycle times

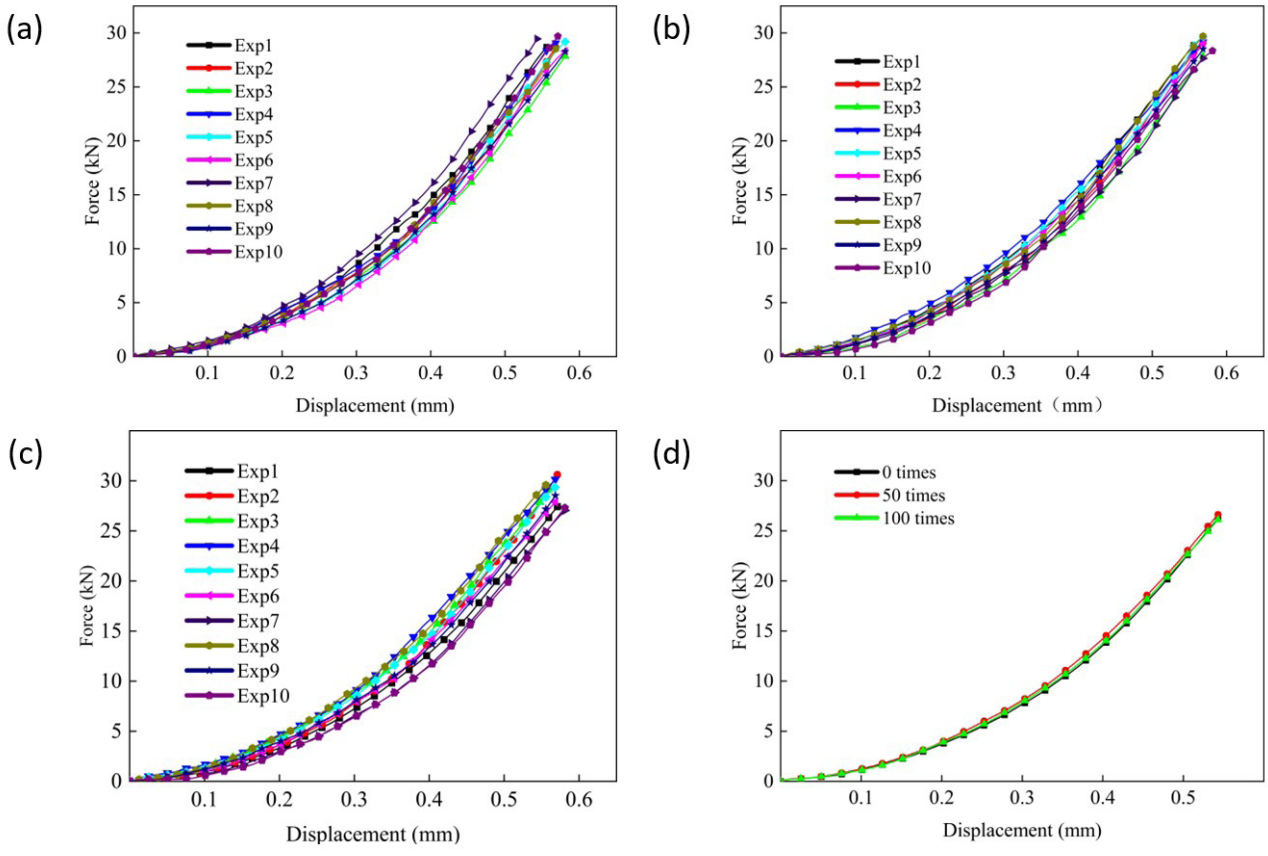

Figure 4 Force-displacement curves of battery separator materials with different cycle times: (a) 0 cycles; (b) 50 cycles; (c) 100 cycles; (a) Comparison of different cycle times

Based on the experimental conditions, finite element analysis models for the anode, cathode, and separator were developed. A schematic of the material-level finite element model is shown in Figure 5(a). The laminated materials were placed between a rigid loading plate and a fixed support plate. The loading speed was 1 mm/min. Referring to the number of layers used in the tests and the modeling approach for battery cathodes, anodes, and separators described in the literature (Qu Y, Xing B, Wang C, et al., 2023), the anode and cathode were each modeled with 20 layers of solid elements, while the separator was modeled with 60 layers. The thickness per layer was 0.2 mm for the anode, 0.17 mm for the cathode, and 0.02 mm for the separator. The mesh size for all three materials is 0.3 mm. Surface-to-surface contact was applied in all models with a friction coefficient of 0.3. The simulations were conducted using the commercial software LS-DYNA, with all three materials modeled as crushable foam, specified by the keyword *MAT_CRUSHABLE_FOAM. The basic material parameters are listed in Table 1, and the compressive behavior curves were calibrated against experimental data, as provided in Table 2. Given that the slope of the average mechanical response of the anode material varied most significantly across 0, 50, and 100 cycles, the influence of cycle number was represented by adjusting the elastic modulus.

Table 1 Main parameters of the cathode, anode and separator

Components	Density	Modulus of elasticity	Poisson's ratio
Cathode	2.520e-09	720	0.01
Anode/0	4.300e-09	300	0.01
Anode/50	4.300e-09	290.8	0.01
Anode/100	4.300e-09	282.5	0.01
Separator	1.200e-09	300	0.15

Table 2 Compressive behavior data of anode material at 0, 50, and 100 Cycles

	Stress/MPa		
Strain	Cathode	Anode	Separator
0.0	0.0	0.0	0.0
0.08	8.0	8.0	8.8
0.16	45.0	26.0	19.8
0.26	108.0	65.0	55.0
0.32	145.0	100.0	90.0
0.5	298.0	168.0	150.0
0.9	350.0	238.0	220.0
0.99	650.0	383.0	250.0
1.01	1200.0	1200.0	600.0

Figures 5(b), (c), and (d) present the finite element simulation results for the cathode, anode, and separator of new batteries, respectively. The simulated force-displacement curves for all three materials show excellent agreement with the experimental data, thereby validating the simplifications in material properties and the effectiveness of the modeling methodology.

2.3 BATTERY CELL EXPERIMENT

In order to better explore the mechanical properties of the battery monomer under different numbers of charge/discharge cycles, indentation tests and flat plate compression tests of the battery are conducted in this subsection. Each test is performed 10 times, primarily focusing on the mechanical behavior of cylindrical lithium-ion batteries at 0% SOC (State of Charge) at 0, 50, and 100 cycles. The aim is to analyze their mechanical behavior under different aging states. A semicircular indenter with a radius of 5 mm is used for the indentation test, while a flat-bottomed indenter is used for the plate compression test. The tests are conducted at a speed of 6 mm/min, and the test process is shown in Figure 6.

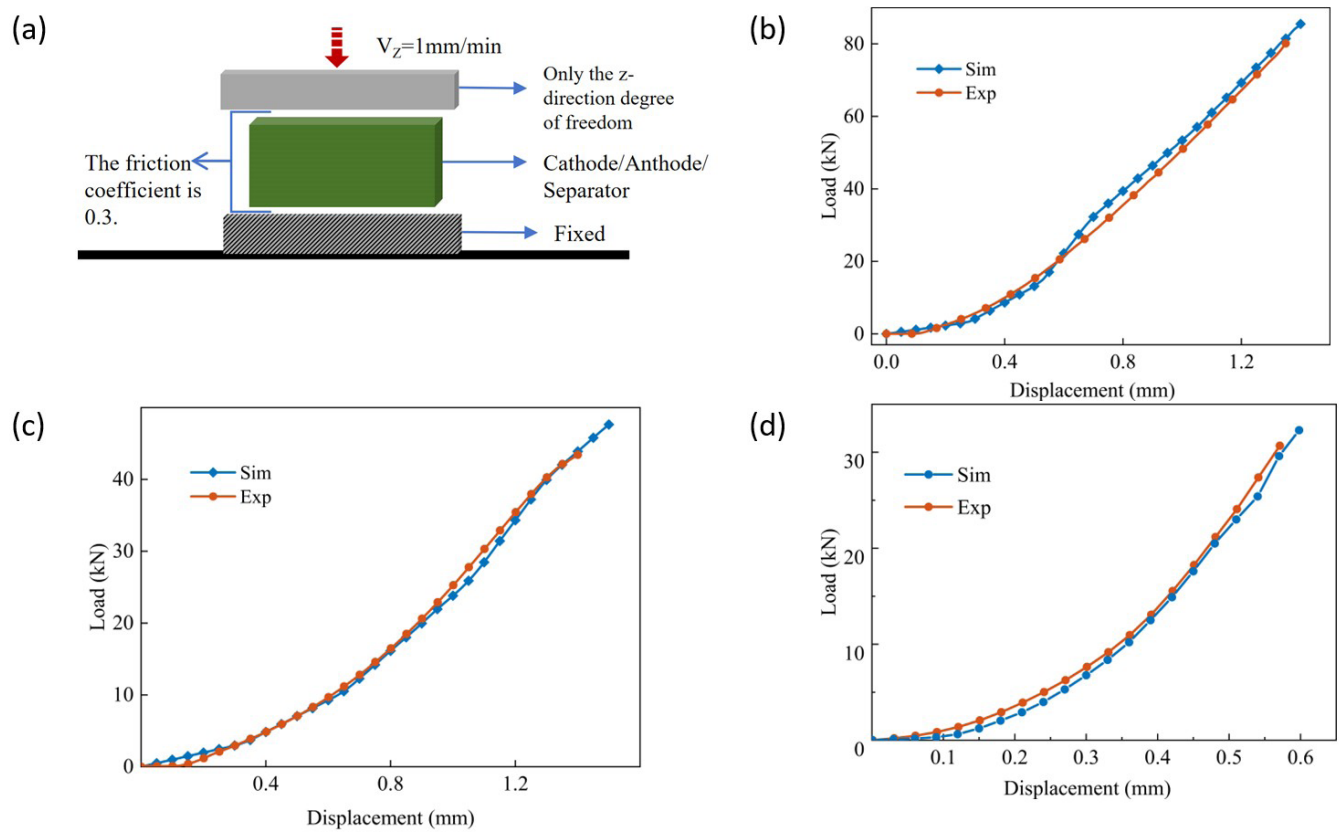

Figure 5 Comparison of cathode, anode and diaphragm simulations and tests. (a) Cathode test and simulation results at 0 cycles; (b) Anode test and simulation results at 0 cycles; (c) Separator test and simulation results at 0 cycles

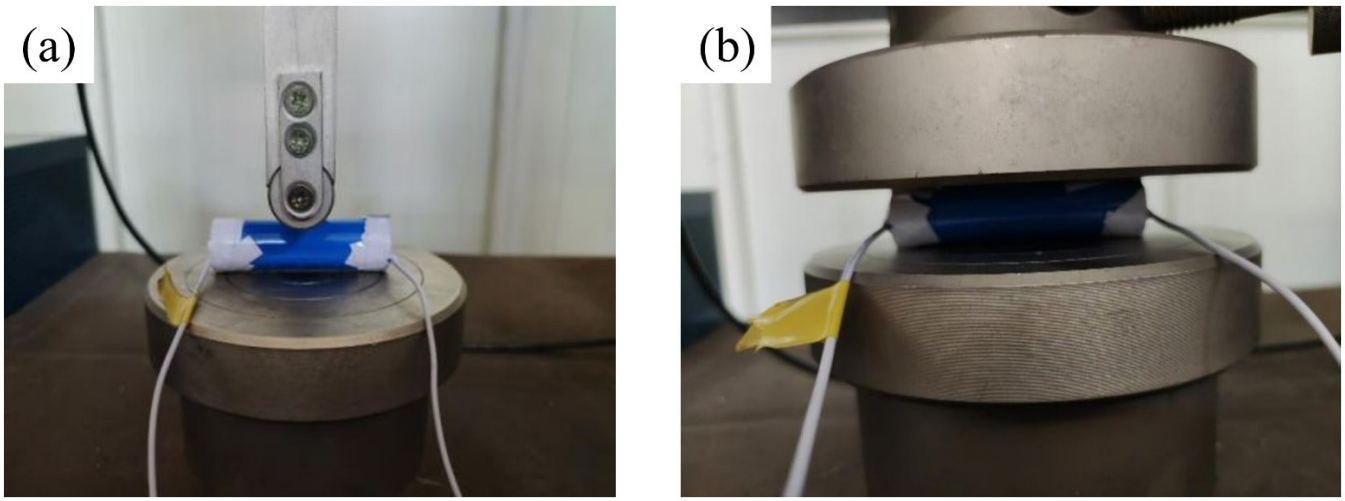

Figure 6 Cell compression test: (a) Indentation test; (b) Flat plate compression test

The force-displacement relationships of indentation tests for batteries with different cycle numbers are shown in Figure 7. The force-displacement curves of indentation tests exhibit an approximately linear increase in the initial stage, followed by a gradual increase in the curve slope until the peak force is reached when the battery fails (Duan X D, Wang H C, et al., 2022). The force-displacement curves of batteries with 0 cycles show high consistency, while the dispersion of curves for batteries with 50 and 100 cycles gradually increases. The average failure displacement of batteries with 0 cycles is approximately 6 mm, that of batteries with 50 cycles is concentrated around 5.7 mm, and that of batteries with 100 cycles is 5.5 mm. The battery failure load decreases significantly from 6.48 kN to 6.29 kN, and then further to 5.95 kN. This indicates that as the number of battery cycles increases, the failure load gradually decreases, reflecting the degradation of the mechanical properties of battery materials. The specific experimental results regarding the failure displacement and failure force for the indentation tests are summarized in Table 3.

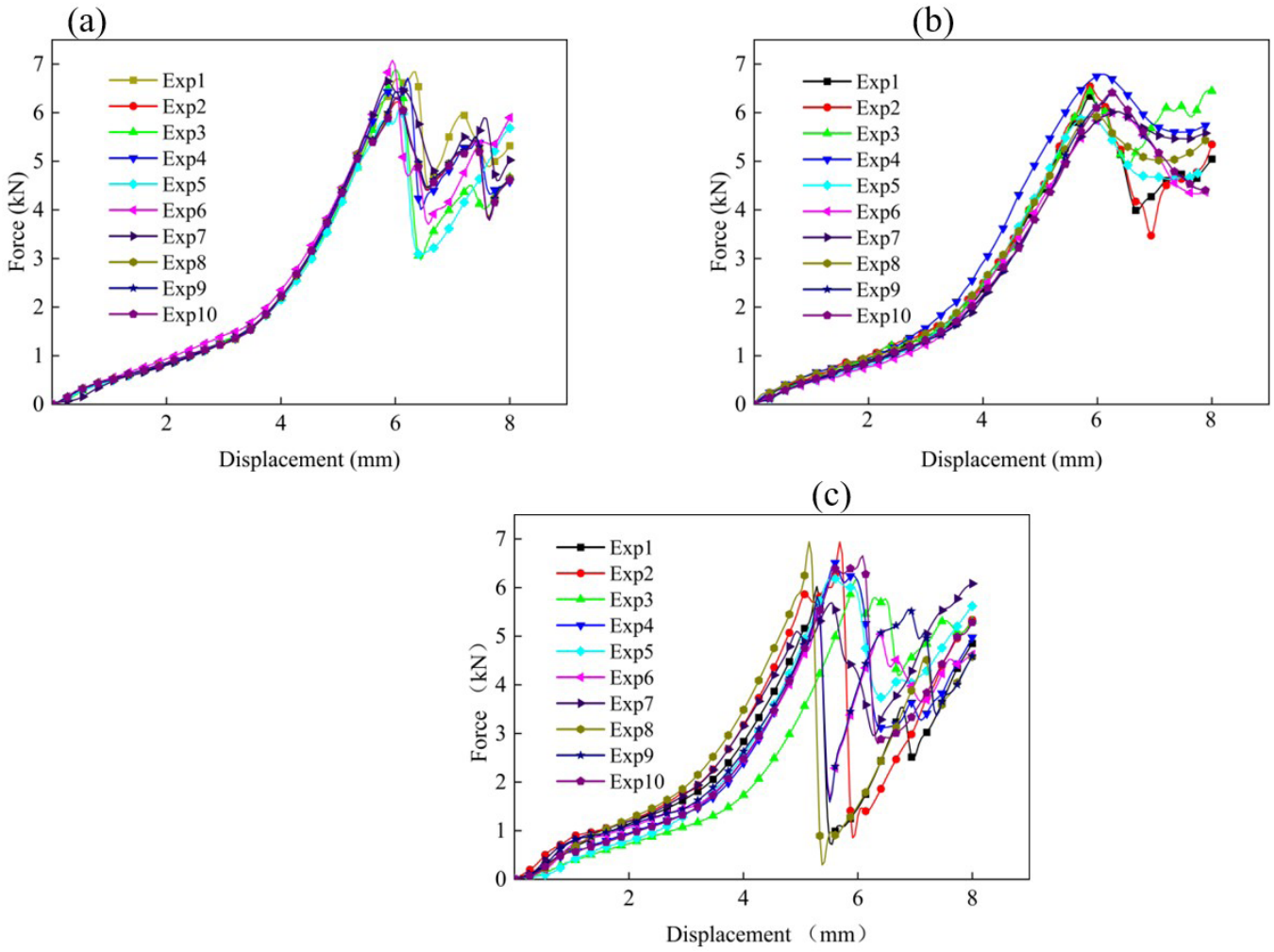

Figure 7 Force-displacement diagram of cell indentation test with different number of cycles: (a) 0 cycles; (b) 50 cycles; (c) 100 cycles

Table 3. Failure displacement and failure force from the indentation tests

	Failure Displacement at 0 Cycles/mm	Failure Force at 0 Cycles/kN	Failure Displacement at 50 Cycles/mm	Failure Force at 50 Cycles/kN	Failure Displacement at 100 Cycles/mm	Failure Force at 100 Cycles/kN
Maximum	6.32	6.89	6.39	6.79	6.00	6.51
Minimum	5.81	5.98	5.85	5.92	5.14	5.34
Average	5.99	6.48	6.07	6.29	5.50	5.95

The force-displacement curves obtained from the flat plate compression tests are shown in Figure 8. It is observed that the overall trend of the force-displacement curves for cells with different numbers of cycles is consistent. The load increases slowly in the displacement range of 0–4 mm. As shown in Table 4, the force-displacement curves tend to shift to the left as the number of cycles increases. The average failure load decreases from 40.655 kN to 35.898 kN, representing about 12% decrease in failure load from 0 to 100 cycles. Concurrently, the average failure displacement decreases from 7.05 mm to 6.9 mm and then to 6.57 mm. These results indicate that the stiffness of the aged cell increases compared to the fresh cell, the failure load of the aged cell decreases significantly compared to the fresh cell, and the failure displacement of the cell advances significantly. Therefore, the aged cell is more prone to failure compared to the fresh cell.

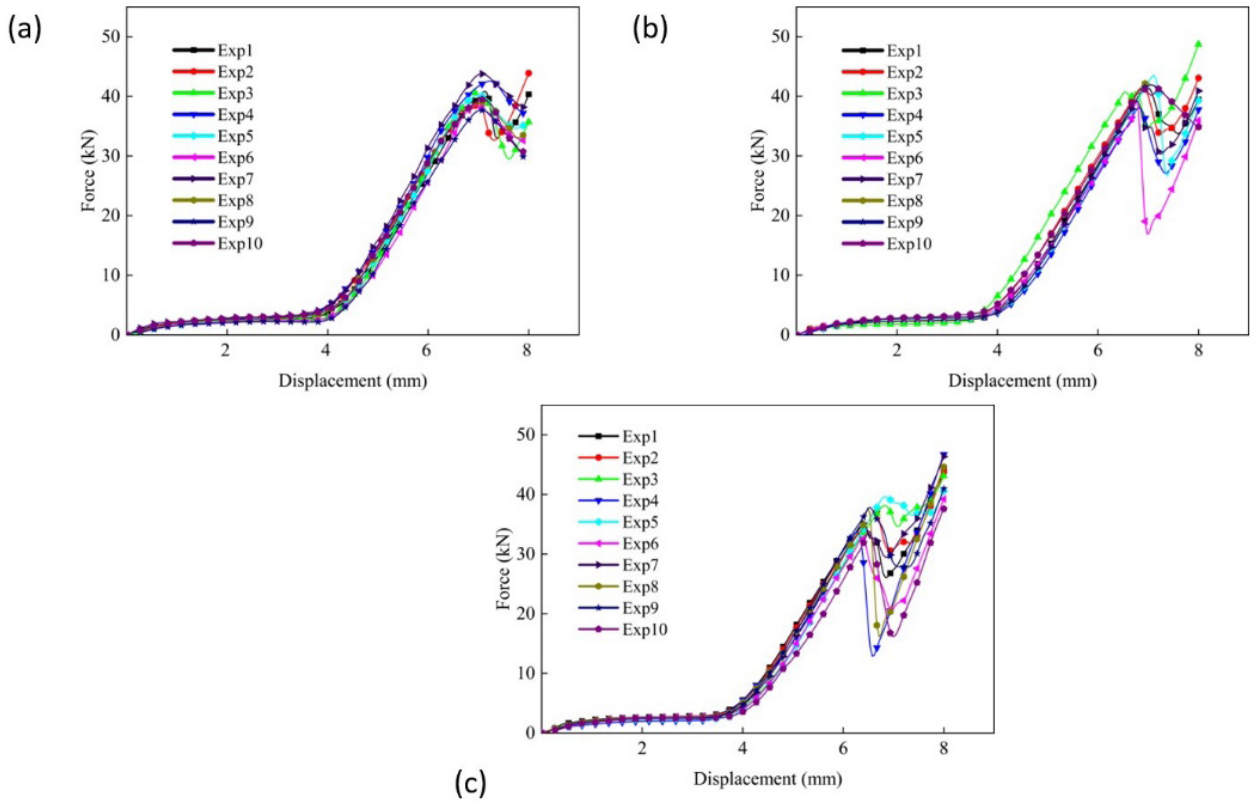

Figure 8 Force-displacement of cell plate compression test with different number of cycles: (a) 0 cycles; (b) 50 cycles; (c) 100 cycles;

Table 4 Failure Displacement and Failure Force from the Plate Test as a Function of Cycle Number

	Failure Displacement at 0 Cycles/mm	Failure Force at 0 Cycles/kN	Failure Displacement at 50 Cycles/mm	Failure Force at 50 Cycles/kN	Failure Displacement at 100 Cycles/mm	Failure Force at 100 Cycles/kN
Maximum	7.212	43.192	7.153	43.759	6.896	39.563
Minimum	6.936	37.671	6.776	37.672	6.356	32.624
Average	7.0476	40.655	6.904	40.050	6.573	35.898

3 COMPUTATIONAL MODELING

3.1 FINITE ELEMENT MODELING

Figure 9 illustrates the structure of the 18650 lithium-ion battery. The outer casing is made of stainless steel, while the internal cell is wound in a repeating sequence of separator–cathode–separator–anode, totaling 76 layers. Accordingly, the wound structure is simplified into 76 concentric circular layers, with each layer representing a separator–cathode–separator–anode unit, arranged sequentially from the inside outward. The thickness of each layer corresponds to that used in the material-level finite element model: 0.17 mm per layer for the cathode, 0.2 mm for the anode, and 0.02 mm for the separator. The material models for each layer are consistent with those defined at the material level, utilizing the *Mat_CRUSHABLE_FOAM constitutive model with parameters as previously determined.

The battery casing is modeled using shell elements, whereas the cathode, anode, and separator are modeled with solid elements. Components such as the safety vent, gasket, and insulating plate at the positive terminal are simplified into a single part and also modeled with solid elements. Table 5 summarizes the element types, mesh sizes, and element counts for each component. To account for the preload present in the actual battery assembly, all internal components are modeled with shared nodes at their interfaces. To ensure nodal compatibility across components, the dimensions of the cathode, anode, and separator were adjusted relative to their material-level models. Contact between the safety vent, cell assembly, and casing is defined using *Contact_Automatic_Surface_To_Surface with a friction coefficient of 0.3.

The material model for the battery casing follows the approach described in the literature (Qu Y, Xing B, Wang C, et al,2023), with parameters calibrated against experimental data. The specific material properties are provided in Table 7. The safety vent is also modeled using *Mat_CRUSHABLE_FOAM, with its material parameters listed in Table 6 and 7.

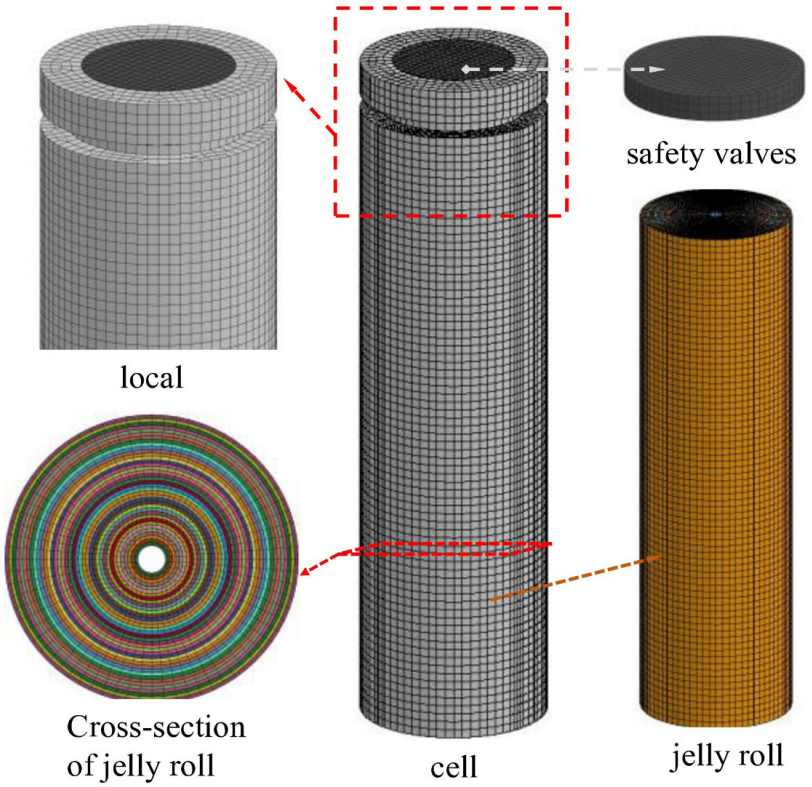

Figure 9 Cell meshing diagram.

Table 5 Mesh division of battery components

Components	Element type	Mesh size (mm)	Element number
Cathode	Solid	0.3-0.8	90750
Anode	Solid	0.3-0.8	88500
Separator	Solid	0.3-0.8	180600
Casing	Shell	0.8	6632
Foam	Solid	0.3-0.8	1194
All			367676

Table 6 Basic parameters for the battery casing and safety vent

	Density(kg/m³)	Elastic Modulus (MPa)	Poisson's Ratio	Yield Strength (MPa)	Tensile Strength (MPa)
Battery casing	7850	211000	0.3	772	781
Safety vent	6500	100	0.3	-----	------

Table 7 Compressive Material Parameters of the Safety Vent

Strain	0.0	0.08	0.15	0.2	0.3	0.4	0.5	0.99	1.01
Stress(MPa)	0.0	8.0	45.0	108.0	145.0	298.0	350.0	650.0	1200.0

As known from the aforementioned experiments, the number of battery cycles has a significant impact on the compressive mechanical properties of the anode material, while the compressive mechanical properties of the cathode material and separator material have no significant correlation with the number of cycles. Therefore, when modeling batteries with different cycle numbers, only the Young's modulus of the anode material needs to be adjusted accordingly.

Figure 10 illustrates the schematic diagrams of the loading and constraint configurations for the plate compression test and the indentation test, respectively. In the plate compression test, the bottom support plate is fixed, while the loading plate moves at a speed of 2 mm/min. For the indentation test, the indenter geometry is consistent with that used in the experimental setup, and the loading speed is also maintained at 2 mm/min.

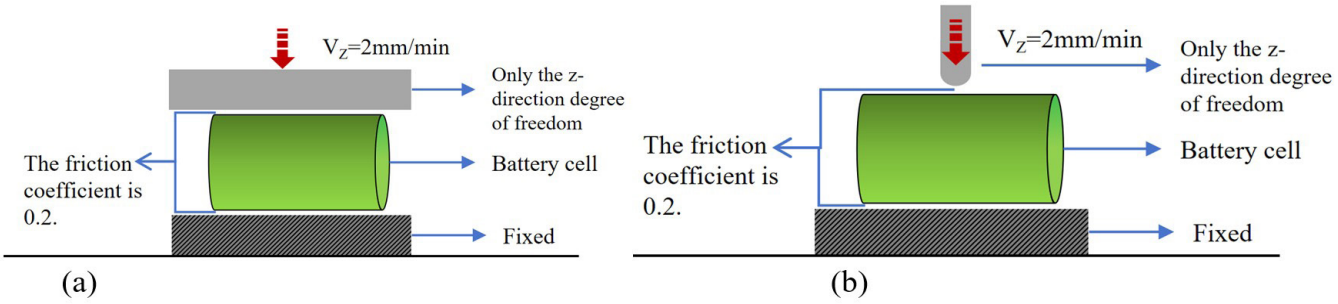

Figure 10 Schematic of the Monocell Plate Compression Test and Indentation Test: (a) Plate Compression; (b) Indentation Test

3.2 BATTERY FAILURE CRITERIA

Similarly, damage to the electrodes may puncture the diaphragm, compromising its insulating properties and triggering a short-circuit, resulting in battery failure. In the compression tests of the battery cathode material and the diaphragm, the slope of the force-displacement curve for the cathode material did not exhibit a change throughout the entire compression test, indicating that the cathode material did not yield or sustain damage. During the compression test of the diaphragm, no yielding was observed.

The internal short-circuit of the battery is considered an important indicator of battery failure. Internal short-circuiting often results from the rupture of the diaphragm, which leads to direct contact between the cathode and anode of the battery(Li Z, Chen J, Lan F, et al,2021).Electrode damage and fragment penetration are among the key factors leading to separator failure. In the compression tests of the cathode material and separator described in Section 2, the slopes of the force-displacement curves for both the cathode and separator remained stable throughout the testing process. In contrast, the anode material exhibited a noticeable change in slope, indicating that the anode is more susceptible to failure under compressive loading.

In the detailed model, failure is determined based on the stress within the anode material layer. The force-displacement curve from the anode compression test shows a peak force, which corresponds to a slope change as the curve approaches this peak. The point exhibiting the greatest reduction in slope near the left side of the peak force is identified as the critical failure point of the anode material for a single test. Based on the experimental results from Section 2, the average forces at the critical failure point for 0, 50, and 100 cycles are 42.5 kN, 36.9 kN, and 29.5 kN, respectively. Given that the laminated anode specimen dimensions are 20 mm × 20 mm, the corresponding stresses are calculated as 106.25 MPa, 94.75 MPa, and 73.75 MPa. These three stress values are adopted as the failure criteria for the anode material under the three cycling conditions.

By adjusting the Young's modulus of the anode material, finite element models of lithium-ion batteries under different cycle numbers were established. Taking the 0-cycle condition as an example, the simulation results for indentation and flat compression of the battery are presented in Figure 11. Only the anode portion is displayed in the figure. In Figure 11(a), the maximum stress reaches 108.9 MPa, while in Figure 11(b), it reaches 110.1 MPa. Both values slightly exceed the failure criterion of 106.25 MPa, indicating that failure can be determined at this stage. The corresponding deformation and force at this point are thus extracted as the failure displacement and failure force, respectively.

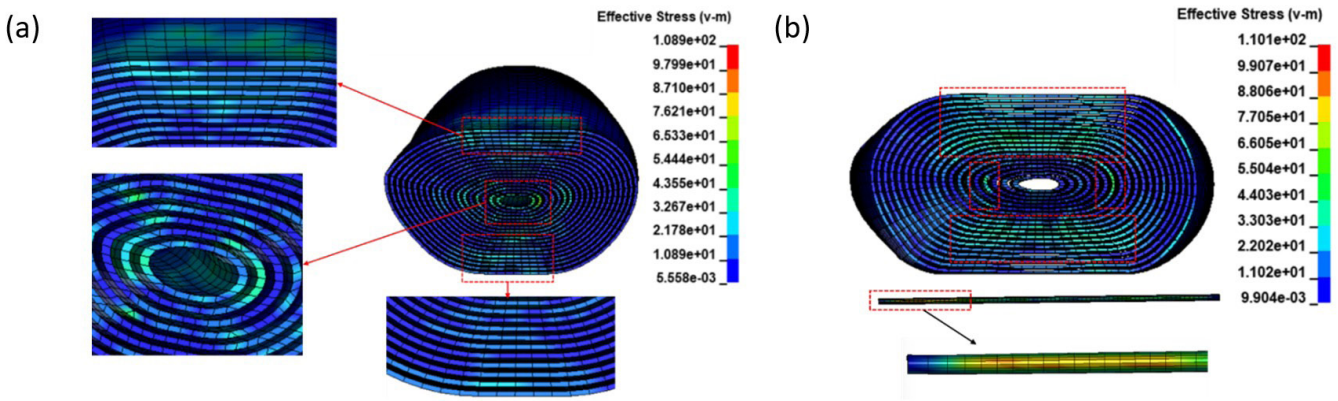

Figure 11 0 cycles battery cell simulation example diagram: (a) 0 cycles - indentation; (b) 0 cycles - flat plate

3.3 SIMULATION RESULTS AND VALIDATION

To verify the accuracy of the improved model, simulations were performed in LS-DYNA with parameter settings identical to those of the experimental tests, ensuring consistency between the simulation parameters and the test process. The indentation and flat compression simulation results for batteries with 0, 50, and 100 cycles were compared with the experimental data, and the detailed comparison results are shown in Figure 12.

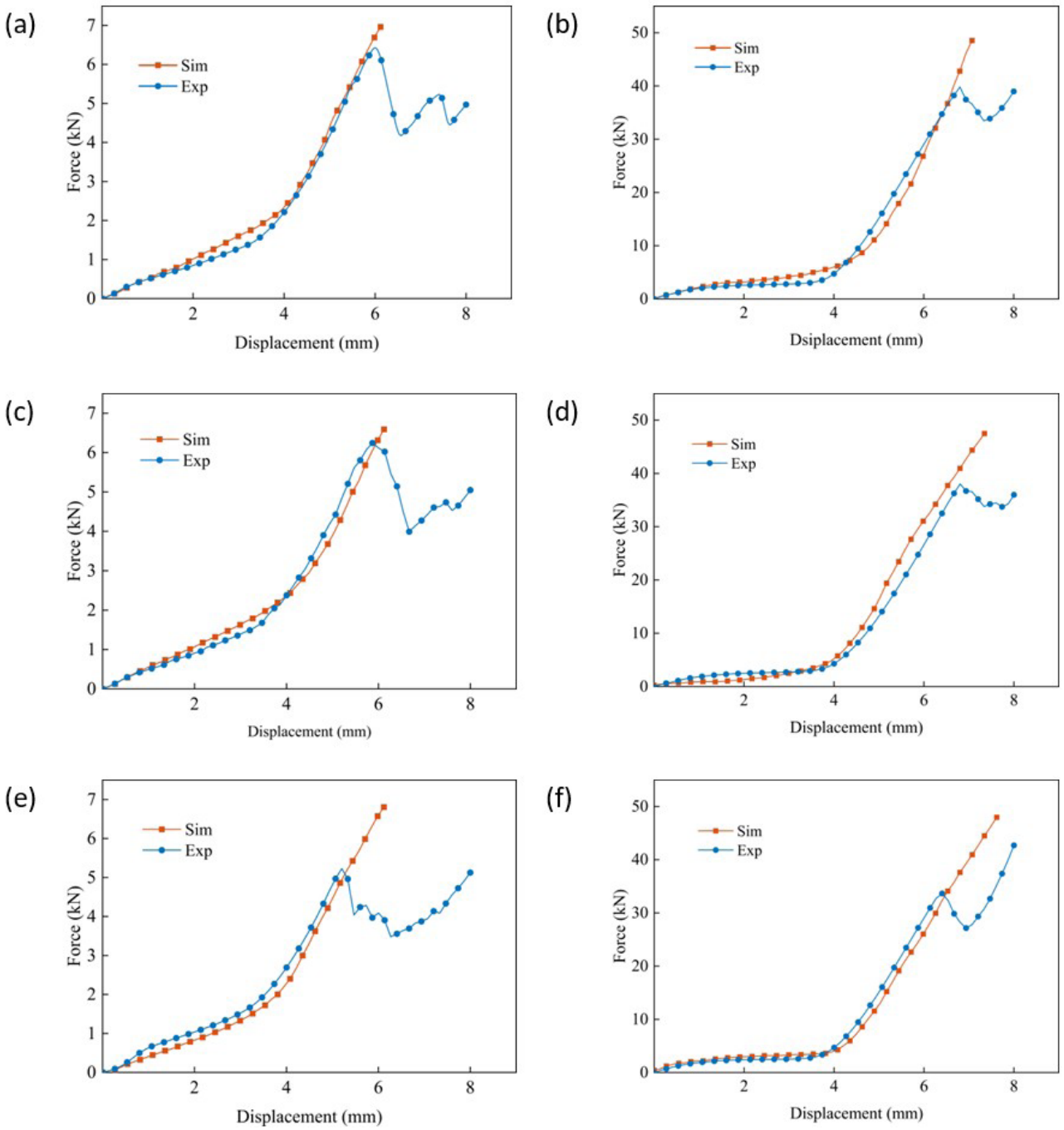

Figure 12 Battery cell simulation example Simulated force-displacement curves: (a) 0 cycles - indentation; (b) 0 cycles - flat plate (c) 50 cycles - indentation (d) 50 cycles - flat plate (e) 100 cycles - indentation (f) 100 cycles - flat plate

As shown in Figure 12, the simulation results accurately capture the overall trend of the experimental data. The simulated force exhibits excellent agreement with the measured values throughout the initial stage of the test up to the peak force. It should be noted that the detailed monocell model was developed specifically for internal stress analysis under deformation boundaries obtained from vehicle-level simulations, rather than for full battery pack crashworthiness assessment in full-vehicle collision models. Consequently, failure criteria were not defined in either the material-level or monocell finite element models. This explains why the force in the finite element model continues to increase beyond the peak force observed in experiments.

The primary purpose of the finite element model is to obtain the internal stress distribution prior to peak force, particularly within the anode layer, for failure assessment. This failure evaluation approach enables the identification of failed cells within the battery pack configuration. Therefore, while the post-peak failure process is not represented in the current model, the focus remains on the accurate replication of the pre-peak stress progression and its consistency with experimental trends.

4 RAPID PREDICTION OF BATTERY CELL CRASH FAILURE

The optimized battery model can accurately characterize the deformation and component failure state of the battery. Lithium-ion battery collision failure involves complex nonlinear mechanical responses, and traditional finite element simulation is time-consuming, making it difficult to quickly meet the demand for predicting a large number of working conditions in engineering design. Given the excellent performance of machine learning methods in various fields (Huang L, Liu L, Lu L, et al., 2021), this study adopts such methods. This research focuses on the scenario where an intruder is pressed into a battery cell laid flat on a rigid surface at a specific angle. Three indenter shapes—rectangular, cylindrical side indenters, and cylindrical bottom indenters—were used to squeeze the battery cells in the experiments. Each indenter type had three different sizes: the rectangular indenters were 10 mm×30 mm, 15 mm×30 mm, and 20 mm×30 mm; the cylindrical side indenters had a length of 30 mm and diameters of 10 mm, 15 mm, and 20 mm respectively; the cylindrical bottom indenters were cylinders with lengths of 20 mm and diameters of 10 mm, 15 mm, and 20 mm. The loading conditions were determined by the loading position and angle, under which the failure load and displacement of the battery cell were the main research indicators.

Therefore, the model developed in this study aims to predict the battery's failure load and failure displacement using five input variables—indenter type, loading position, indenter size, loading angle, and battery cycle number—classifying this problem as a regression task. Machine learning models excel at handling regression problems, with neural networks being particularly suitable for addressing such regression challenges. However, training the model requires a large volume of data. Acquiring data through physical experiments is both time-consuming and costly; thus, the training data are derived from simulation experiments.

4.1 SIMULATION MATRIX DESIGN AND RESULTS

Simulations are conducted under three distinct conditions involving the indenter. Figure 13 illustrates the various intrusion scenarios: vertical and tilted on the cylindrical side, on the cylindrical bottom surface, and on the rectangular surface. The locations where the load is applied are marked as points 1 through 5, situated at 10, 15, 20, 25, and 30 mm away from the cell's cathode, respectively. The simulation matrices corresponding to these conditions are presented in Table 8. The simulation conditions in the table are for localized indentation and can be designed in a similar way for other types of indenters and compression methods.

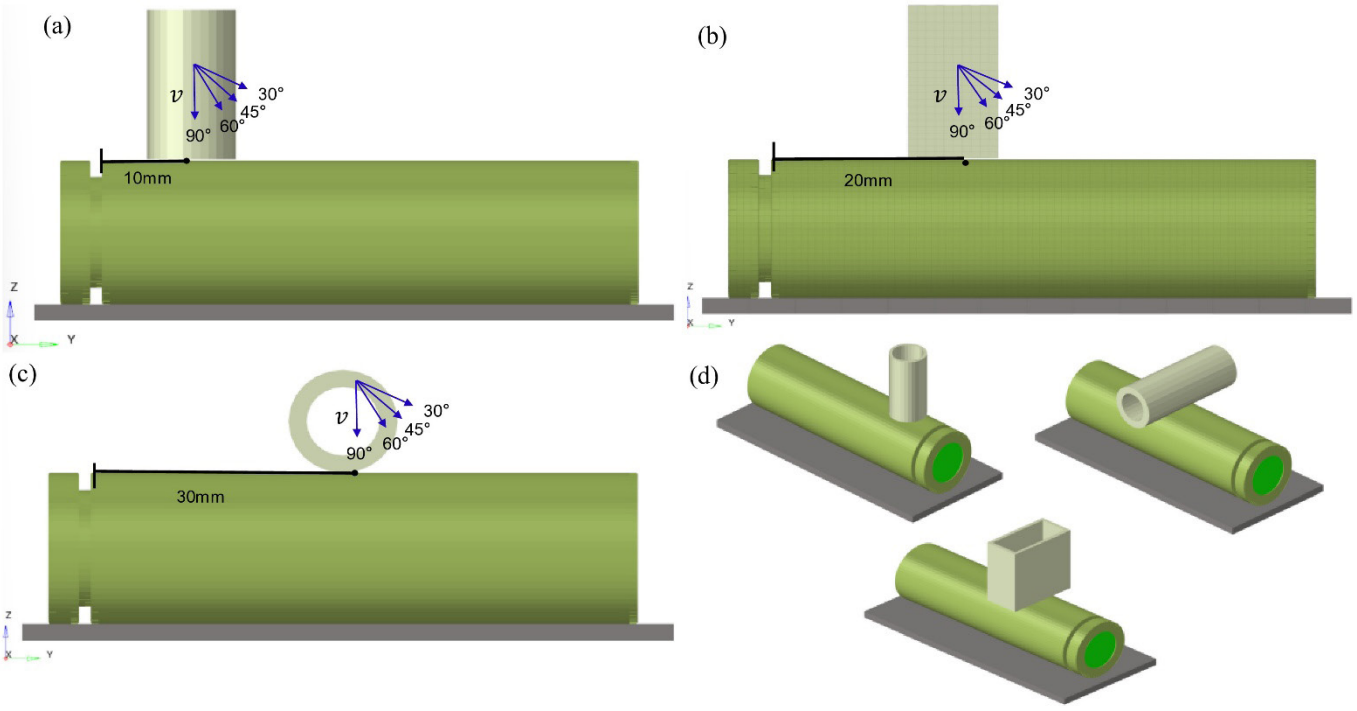

Figure 13 Design of different simulation conditions: (a) Round bottom indenter loaded at position 1; (b) Rectangular face indenter loaded at position 3; (c) Cylindrical side indenter loaded at position 5; (d) Three indenter loading conditions

Table 8 Design of simulation matrix

Type of intruder		cylindrical-side		cylindrical-bottom		rectangular
Size of intruder	mm	10		15		20
Angle of invasion	degree	30°	45°		60°	90°
Intrusion Location		1	2	3	4	5
Cycle times		0		50		100
General simulation example 3×3×3×4×5=540						

Using LS-DYNA to solve each simulation case, the collated test results are shown in Figure 13 to clearly illustrate the influence of each factor on the failure load and failure displacement of the battery monomer. The failure displacement and load are determined based on whether the maximum stress in the anode material layer reaches the critical stress value. When the maximum stress in the simulation results meets or exceeds the critical stress, the corresponding indenter displacement and interaction force at that moment are recorded as the failure displacement and failure load, respectively.

In Figure 14(a), the horizontal coordinates 1, 2, and 3 indicate the rectangular surface indenter, cylindrical bottom indenter, and cylindrical side indenter, respectively. In Figure 14(b), the horizontal coordinates indicate the distance from the cathode of the battery to the loading position of the indenter. In Figure 15(c), the horizontal coordinates indicate the dimensions of the indenter. In Figure 14(d), the horizontal coordinates indicate the angle of the loading of the indenter. The horizontal coordinate in Figure 14(e) indicates the number of cycles of the battery.

Clearly, the failure displacement and failure load of the battery are significantly affected by the type of indenter. The loading position of the indenter has a smaller effect on the failure displacement, and the failure load decreases as the loading position moves from the vicinity of the battery cathode to the center part of the battery. The failure load is linearly related to the size of the indenter, and the failure displacement increases slightly with the size of the indenter. With the increase of the loading angle, the failure load and displacement also increase. This may be due to the fact that when the loading angle is less than 90°, the sharp edges of the indenter may puncture the battery shell, leading to premature failure of the battery. Additionally, the number of cycles of the battery is significantly correlated with the failure load and failure displacement. As the number of cycles of the battery increases, the failure displacement gradually decreases and the failure load gradually increases.

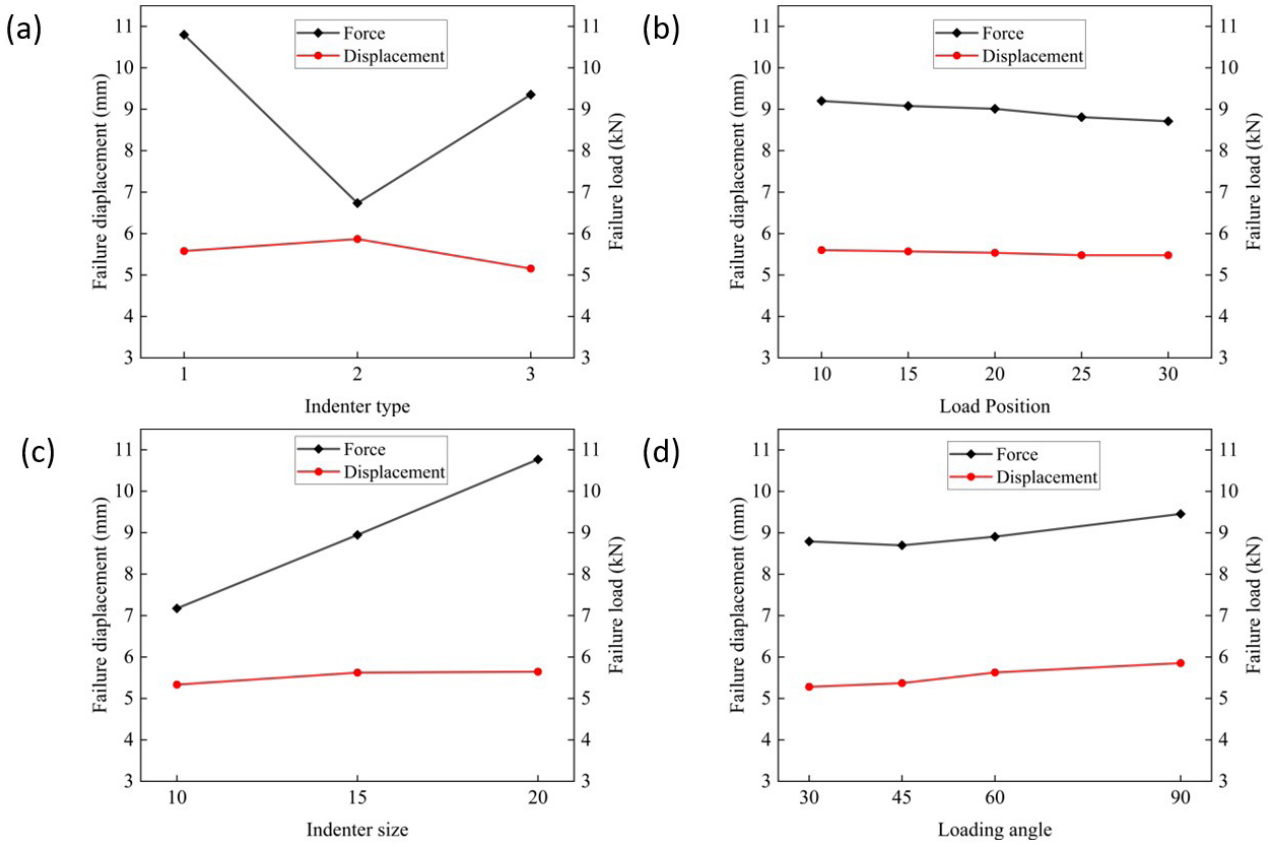

Figure 14 Failure displacements and loads for different simulation conditions: (a)Different indenter types; (b)Different loading positions; (c)Different indenter sizes; (d)Different loading angles; (e)Different number of cycles

4.2 MODEL BUILDING PROCESS AND ANALYSIS OF TRAINING RESULTS

The use of three types of indenters means three different loading modes. Here, a unique thermal coding format is used to represent the rectangular, cylindrical side, and cylindrical bottom indenters, respectively. The code (1, 0, 0) represents the rectangular indenter, the code (0, 1, 0) represents the cylindrical bottom indenter, and the code (0, 0, 1) represents the cylindrical side indenter. The different numbers of cycles of the battery are normalized: the 0-cycle battery is represented using code 0, the 50-cycle battery using code 0.5, and the 100-cycle battery using code 1. Thus, the model has a total of 7 inputs and 2 outputs. The number of neurons in the input layer is 7, the number of neurons in the hidden layer is set to 128, and the number of neurons in the output layer is 2. Specifically, the type of indenter is input to the first three neurons in the input layer, the position of loading is input to the fourth neuron, the size of the indenter is input to the fifth neuron, the angle of loading is input to the sixth neuron, and the number of cycles of the battery is input to the seventh neuron. The neurons in the output layer output the failure load and failure displacement.

The model underwent training with 432 sets of data, constituting 80% of the total, while 108 sets of data, representing 20%, were employed for testing. Given that the model's input parameters varied significantly in magnitude, normalization of the input data was essential to foster quicker and more effective convergence of the model. The normalization process is outlined in Equation (1).

$$X = \frac{x - x_{mean}}{x_{max} - x_{min}} \tag{1}$$

Where X represents the normalized data, x denotes the un-normalized data, is the mean value of the data set undergoing normalization, and are the maximum and minimum values within the data set, respectively. The entirety of this normalization process is depicted in Figure 15.

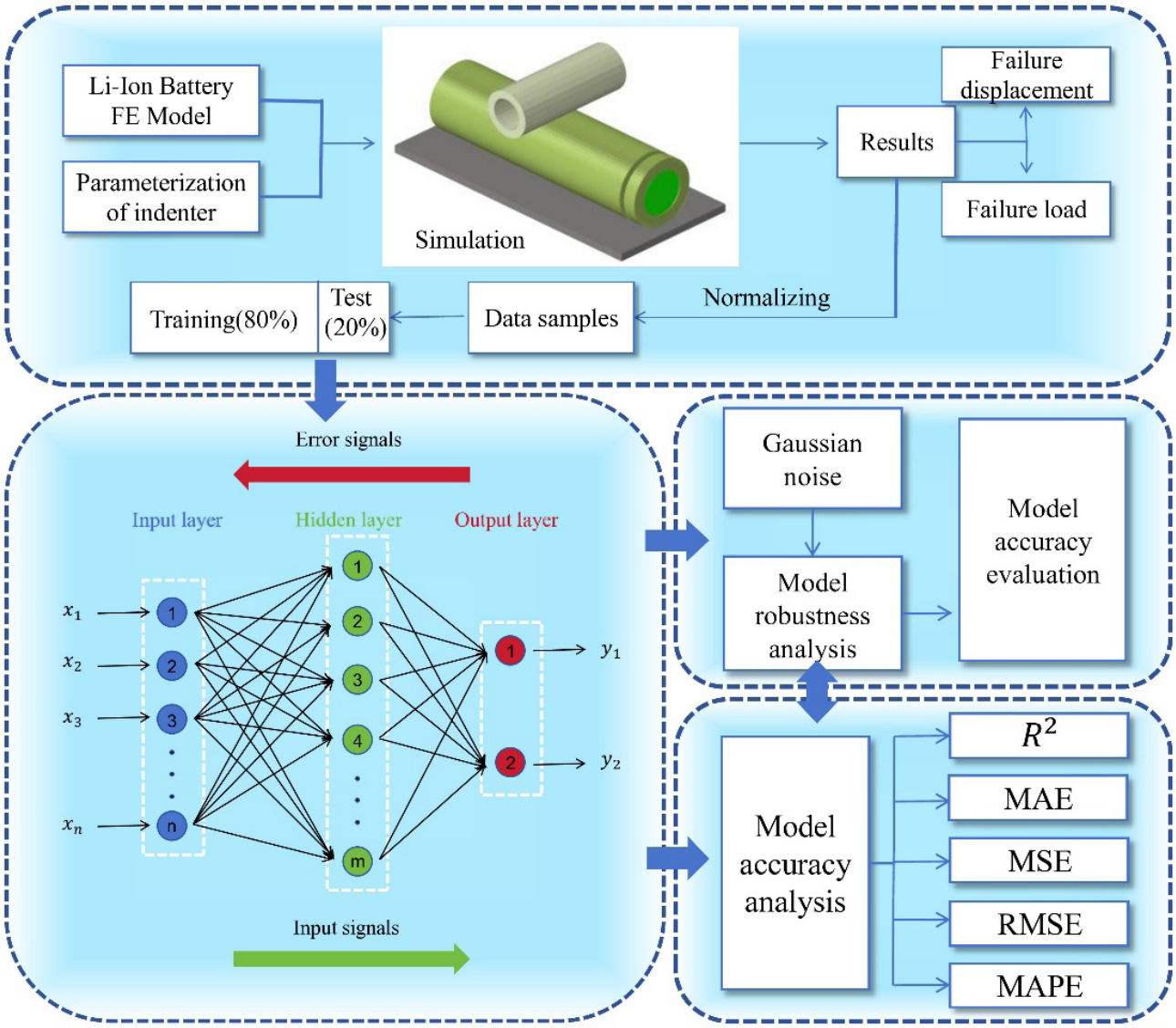

Figure 15 Complete flow chart for modeling.

The machine learning (ML) model is utilized to conduct failure load and failure displacement prediction analyses of lithium-ion batteries under various indentation conditions. One-third of the data is extracted for visual evaluation, and the results are presented in Figure 16. The horizontal axis represents the number of samples in the test set, the left Y-axis indicates the failure displacement in mm, and the right Y-axis indicates the failure load in kN. It is evident that the prediction results of the ML model closely align with the analysis results of the finite element (FE) model.

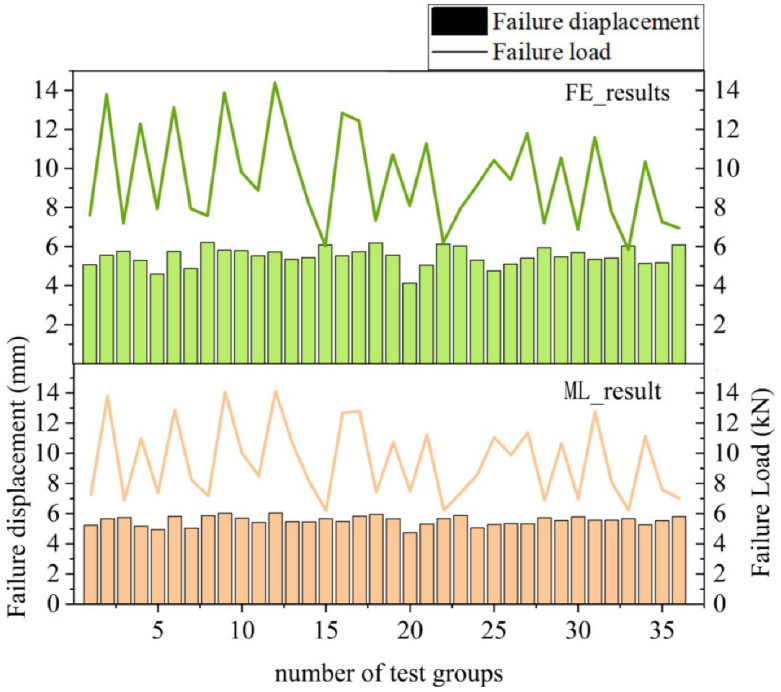

Figure 16 Comparison of machine learning model prediction results with simulation results.

4.3 ANALYSIS OF MODEL ROBUSTNESS

To conduct a comprehensive evaluation of the machine learning (ML) model, five metrics were employed for result comparison(Pan Y, Sun Y, Li Z, et al,2023). These included the coefficient of determination, mean square error (MSE), root mean square error (RMSE), mean absolute error (MAE), and mean absolute percentage error (MAPE). In addition, the model's robustness was evaluated by adding Gaussian noise with a zero mean and standard deviations of 0.05, 0.1, and 0.2 to the test data. This1 process served to mimic errors potentially occurring during sampling (Xu D, Pan Y, Zhang X, et al,2024;Rautela M, Gopalakrishnan S,2021). Subsequent predictions were made using the trained model, and the evaluation results are presented in the table 9. It was observed that the model exhibited solid robustness. Even when subjected to the highest level of error, the MAPE merely reached 6.72%, whereas the MAPE for the original data without noise is 3.38%.

Table 9 Evaluation results of the model

		MSE	RMSE	MAE	MAPE
Original data	0.9840	0.1132	0.3364	0.2532	3.38%
Original data + Gaussian noise(0.05)	0.9824	0.1242	0.3525	0.2761	3.68%
Original data + Gaussian noise(0.1)	0.9615	0.2722	0.5218	0.3711	4.95%
Original data + Gaussian noise(0.2)	0.9233	0.6778	0.8233	0.5031	6.72%

5 CONCLUSION

This study presents an integrated finite element and machine learning framework for crash-induced failure prediction of 18650 lithium-ion batteries, addressing the computational limitations of traditional simulation approaches in engineering applications. The principal findings are summarized as follows:

Through comprehensive mechanical testing of battery components and single cells across 0 to 100 cycle counts, a refined finite element model with a 76-layer structure was developed and validated. The model demonstrates excellent capability in capturing the mechanical response of battery cells under both indentation and flat-plate compression conditions.
A physics-based failure criterion was established using the critical stress state of anode material, derived from experimental characterization. Implementation of this criterion in simulation enabled determination of failure loads and displacements across various indentation scenarios.
A machine learning model was developed for rapid failure prediction, achieving high accuracy across five performance metrics. The model maintains robust performance under noisy conditions.

Acknowledgments

This research has been supported by the Major Science and Technology Project of Jilin Province and Changchun City (grant no.20240301010ZD).

Author's Contributions: Project administration, Yan Ma; Formal analysis, Hongjun He; Investigation, Ning Wang; Resources, Hongbin Tang;Data curation,Hongxin Xia; Conceptualization and Methodology, Guang Chen; Software, Zhongyuan Song; Validation, Wenshuo Chen.

Data availability statement: Research data is only available upon request

Editor: Pablo Andrés Muñoz Rojas

References

Feng X, Ouyang M, Liu X, et al. Thermal runaway mechanism of lithium ion battery for electric vehicles: A review[J]. Energy storage materials, 2018, 10: 246-267.

Lai W J, Ali M Y, Pan J. Mechanical behavior of representative volume elements of LIBs modules under various loading conditions[J]. Journal of Power Sources, 2014, 248: 789-808.

Sahraei E, Bosco E, Dixon B, et al. Microscale failure mechanisms leading to internal short circuit in Li-ion batteries under complex loading scenarios[J]. Journal of Power Sources, 2016, 319: 56-65.

Sahraei E, Kahn M, Meier J, et al. Modelling of cracks developed in lithium-ion cells under mechanical loading[J]. Rsc Advances, 2015, 5(98): 80369-80380.

Zhang C, Xu J, Cao L, et al. Constitutive behavior and progressive mechanical failure of electrodes in LIBs[J]. Journal of Power Sources, 2017, 357: 126-137.

Zhang X, Sahraei E, Wang K. Deformation and failure characteristics of four types of LIBs separators[J]. Journal of Power Sources, 2016, 327: 693-701.

Duan X, Wang H, Jia Y, et al. A multiphysics understanding of internal short circuit mechanisms in LIBs upon mechanical stress abuse[J]. Energy Storage Materials, 2022, 45: 667-679.

Wierzbicki T, Sahraei E. Homogenized mechanical properties for the jellyroll of cylindrical Lithium-ion cells[J]. Journal of power sources, 2013, 241: 467-476.

Chung S.H, Tancogne J, Zhu,H. Failure in LIBs under transverse indentation loading[J]. Power Sources. 2018, 389: 148–159.

Luo H, Xia Y, Zhou Q. Mechanical damage in a lithium-ion pouch cell under indentation loads[J]. Power Sources. 2017, 357: 61–70.

Li W, Xing B, Watkins T R, et al. Damage of prismatic lithium-ion cells subject to bending: Test, model, and detection[J]. EcoMat, 2022, 4(6): e12257.

Avdeev I, Gilaki M. Structural analysis and experimental characterization of cylindrical LIBs cells subject to lateral impact[J]. Journal of Power Sources, 2014, 271: 382-391.

Zhang C, Santhanagopalan S, Sprague M A, et al. Coupled mechanical-electrical-thermal modeling for short-circuit prediction in a lithium-ion cell under mechanical abuse[J]. Journal of Power Sources, 2015, 290: 102-113.

Zhu J, Zhang X, Sahraei E, et al. Deformation and failure mechanisms of 18650 battery cells under axial compression[J]. Journal of Power Sources, 2016, 336: 332-340.

Kulkarni S S, Vysoudil F, Vietor T. Evaluation of Modelling and Simulation Strategies to Investigate the Mechanical Integrity of a Battery Cell Using Finite Element Methods[J]. Energies, 2021, 14(11): 2976.

Li W, Zhu J, Xia Y, et al. Data-driven safety envelope of LIBs for electric vehicles[J]. Joule, 2019, 3(11): 2703-2715.

Wang L, Yin S, Yu Z, et al. Unlocking the significant role of shell material for LIBs safety[J]. Materials & Design, 2018, 160: 601-610.

Li Z, Chen J, Lan F, et al. Constitutive behavior and mechanical failure of internal configuration in prismatic LIBs under mechanical loading[J]. Energies, 2021, 14(5): 1219.

Wang P, Chen J, Li Z, et al. Mechanical Failure Modes of Prismatic LIBs Separator[R]. SAE Technical Paper, 2022.

Fu R, Xiao M, Choe S Y. Modeling, validation and analysis of mechanical stress generation and dimension changes of a pouch type high power Li-ion battery[J]. Journal of Power Sources, 2013, 224: 211-224.

Qi Y, Guo H, Hector L G, et al. Threefold increase in the Young's modulus of graphite negative electrode during lithium intercalation[J]. Journal of The Electrochemical Society, 2010, 157(5): A558.

Qu Y, Xing B, Wang C, et al. Simplified layered model of pouch cell for varied load cases: an indentation and three-point bending study[J]. Journal of Energy Storage, 2023, 59: 106476.

Li Z, Chen J, Lan F, et al. Constitutive behavior and mechanical failure of internal configuration in prismatic lithium-ion batteries under mechanical loading[J]. Energies, 2021, 14(5): 1219.

Huang L, Liu L, Lu L, et al. A review of the internal short circuit mechanism in lithium-ion batteries: Inducement, detection and prevention[J]. International Journal of Energy Research, 2021, 45(11): 15797-15831.

Pan Y, Sun Y, Li Z, et al. Machine learning approaches to estimate suspension parameters for performance degradation assessment using accurate dynamic simulations[J]. Reliability Engineering & System Safety, 2023, 230: 108950.

Xu D, Pan Y, Zhang X, et al. Data-driven modelling and evaluation of a battery-pack system's mechanical safety against bottom cone impact[J]. Energy, 2024, 290: 130145.

Rautela M, Gopalakrishnan S. Ultrasonic guided wave based structural damage detection and localization using model assisted convolutional and recurrent neural networks[J]. Expert Systems with Applications, 2021, 167: 114189.

Du H, Deng Y, Xue J, et al. Robust online CSI estimation in a complex environment[J]. IEEE Transactions on Wireless Communications, 2022, 21(10): 8322-8336.